Mathematical modeling and numerical simulation of magnetic susceptibility artifacts in Magnetic Resonance Imaging

S. Balac[1] and G. Caloz[2]

[1] Département de Mathématiques, Université de Bretagne Occidentale, 29285 Brest, France (Stephane.Balac@univ-brest.fr)

[2] Institut de Recherche Mathématiques de Rennes, Université de Rennes 1, 35042 Rennes, France (Gabriel.Caloz@univ-rennes1.fr)

Abstract

The technique used to spot information in Magnetic Resonance Imaging (MRI) is based on electromagnetic fields. To a strong homogeneous magnetic field (order of magnitude around one Tesla) is added a linearly varying field (around 10^{-2} Tesla per meter). When these fields are disturbed by the presence of a paramagnetic material in the sample for instance, the resulting image is usually distorted, these distortions are called artifacts. Our goal is to present a method, assuming the field disturbances are known, to construct the images. A mathematical model of the MRI process is developed. The way the images are distorted in intensity and shape is explained and an algorithm to simulate magnetic susceptibility artifacts is deduced.

Keywords: Mathematical modeling, numerical simulation, magnetic resonance imaging, biomedical implant, artifact

1 Introduction

The Magnetic Resonance Imaging (MRI) technique requires a strong uniform magnetic field $\boldsymbol{B_0}$ (order of magnitude around one Tesla) to magnetize the sample. Then magnetic field gradients, which are magnetic fields with a linearly varying intensity (around 10^{-2} Tesla per meter), are applied to select a slice of the sample to be imaged, this ensures part of the spatial encoding of the MRI signal.

Any perturbation of the gradients can disturb the imaging process and then render the resulting image inaccurate. Sources of perturbations are various. First of all the static field $\boldsymbol{B_0}$ and the applied gradients are not exactly uniform. However these defects are properties of the MRI device and they are minimized and taken into account in the reconstruction algorithms, see for instance [Weis & Budinsky, 1990] or [Abele *et al*, 1994]. Another cause for magnetic field perturbation is strong tissue magnetic susceptibility variations (as near air sinuses). [Bhagwandien *et al*, 1994] and [Li *et al*, 1995] investigate the distortion of the static magnetic field in 2D anatomical models using the finite difference method and the finite element method. A common cause for magnetic field perturbations is the presence

This work was carried out within the framework of the research group G.I.S. biomatériaux métalliques at the University of Rennes 1, France.

of an object, like a metallic biomedical implant, with magnetic properties different from the ones of the surrounding tissue. As well metallic surgical instruments used in MRI guided surgery are liable for magnetic field perturbations. These perturbations depend on the position, size, shape, and magnetic susceptibility of the metallic objects involved. They can be very important especially near the metallic device which is often the region of interest in the image. The resulting distortions in the image are known as magnetic susceptibility artifacts.

There are various solutions that can be used either to remove or to reduce magnetic susceptibility artifacts. One would be to design new medical implants which possess magnetic properties such that the magnetic field induced would be almost zero, canceling the artifact effect, see [Chauvel *et al*, 1996]. To develop new medical implants numerous experiments need to be carried out. Numerical simulation appears to be a valuable tool to investigate this approach. To perform it it is necessary to solve two distinct problems. The first one is to compute the magnetic field disturbances due to the medical implant. The second one is to use the resulting computations of field disturbances to obtain the image distortions. In the past several studies have been undertaken in that direction, see [Ludeke *et al*, 1985], [Ericsson *et al*, 1988] or [Bakker *et al*, 1993], in the attempt to construct numerical simulation methods. However these studies suffer from too limitative assumptions on the implant geometry as well as on the algorithm used to simulate the image distortions. We have developed a computational procedure to calculate the magnetic field perturbations induced by a paramagnetic body of general shape, see [Balac & Caloz, 1996], [Balac & Caloz, 1998]. Now in this paper a model is presented from which we deduce an algorithm to construct the image distortions. First a precise mathematical model of the MRI imaging process is made out. Then this model is upgraded to take into account the magnetic field inhomogeneities. It allows to derive algorithms for numerical simulation. Moreover it enables to find again the well known effects of magnetic perturbations on an MRI experiment, as described in standard textbooks, and to accurately quantify the various distortions giving rise to the artifact. Finally we have developed a software to simulate the artifacts for implants of very general shape with two basic MRI sequences, namely the Spin-Echo sequence and the Gradient-Echo sequence.

Another approach to study magnetic susceptibility artifacts would be to model the MRI sequences via the Bloch equations. In that direction [Olsson *et al*, 1995] propose a computer simulation program to investigate magnetic susceptibility artifacts under various imaging sequences. The basic idea is to solve repeatedly the Bloch equations for each voxel of the object and for a given pulse sequence to get the magnetization vector. Then the image is obtained through a Fourier transform of the sampled signal. This method is in a certain sense more precise than ours to deal with various imaging sequences and parameters. But its implementation and use are by far much more involved. For each voxel the Bloch equations need to be solved and it is very costly to get a good resolution image. The two approaches are quite different but appear to be complementary.

Our paper is organized as follows. In Section 2 we present a mathematical model of the MRI imaging process. In Section 3 the model is upgraded to take into account magnetic field inhomogeneities. Section 4 is devoted to an analysis of the model; in particular we explain how magnetic field inhomogeneities give rise to image distortions. Finally in Section 5 we present algorithms to simulate magnetic susceptibility artifacts and numerical experiments with a dental implant.

2 The principle of nuclear magnetic resonance imaging

When certain atomic nuclei are placed in a magnetic field $\boldsymbol{B_0}$ and stimulated by a radio frequency pulse (RF pulse) $\boldsymbol{B_1}$, they re-emit some of the absorbed energy as a radio-signal. This phenomenon is known as Nuclear Magnetic Resonance (NMR) and the collected signal is the NMR signal. For sensitivity reason MRI concerns mainly the study of hydrogen nucleus. The frequency of the RF pulse by which a given nuclear species (characterized by its gyromagnetic ratio γ) is stimulated (we say that the nuclei *resonate*) is expressed by the Larmor relation

$$\nu_L = \frac{\gamma}{2\pi} B, \tag{2.1}$$

where B is the modulus of the applied magnetic field. The Larmor relation (2.1) also gives the frequency of the NMR signal.

By analyzing the NMR signal, information about the nucleus density and the chemical composition of the sample is obtained. However this information is integrated over the whole sample. In order to localize where the information is coming from and to get an *image* of the sample, a *spatial encoding* of the NMR signal is needed. The tools for spatial encoding are the magnetic field gradients.

2.1 Magnetic field gradients

In the MRI terminology a gradient is a magnetic field applied along the same direction as the main static field $\boldsymbol{B_0}$ but with a strength that depends linearly on the position. The gradient field strength is much weaker than the one of $\boldsymbol{B_0}$, about 10^4 times. The major characteristic of a gradient field is the linear variation in its strength along one direction only, the other two directions being not affected. In the sequel the variation direction will be referred as the *gradient direction* and the linear variation coefficient as the *gradient intensity*. Let g denotes the gradient intensity, $\boldsymbol{n}$ its direction, $\boldsymbol{r} = \boldsymbol{OP}$, then the gradient field is expressed by

$$\boldsymbol{G}(P) = g(\boldsymbol{r} \cdot \boldsymbol{n})\boldsymbol{z}; \tag{2.2}$$

here we will refer to the laboratory coordinate system $(O, \boldsymbol{x}, \boldsymbol{y}, \boldsymbol{z})$ where $\boldsymbol{z}$ is defined by the direction of $\boldsymbol{B_0}$ (i.e. $\boldsymbol{z}$ is along the bore of the magnet) and the two other directions $\boldsymbol{x}$ and $\boldsymbol{y}$ are taken arbitrarily.

2.2 Slice selection process

Assume we want to get the image of a plane cross section Π_s through the sample. Let $\boldsymbol{n_s}$ be a unit vector normal to the plane and let C be the point belonging to Π_s such that $\boldsymbol{OC} = c\,\boldsymbol{n_s}$, see Figure 1. To select the plane Π_s a gradient $\boldsymbol{G_s}$ called *the slice selection gradient* is turned on when applying the RF pulse $\boldsymbol{B_1}$. The gradient direction is $\boldsymbol{n_s}$ and for $P \in \Pi_s$ it is expressed as

$$\boldsymbol{G_s}(P) = g_s(\boldsymbol{OP} \cdot \boldsymbol{n_s})\boldsymbol{z} = g_s\left((\boldsymbol{OC} + \boldsymbol{CP}) \cdot \boldsymbol{n_s}\right)\boldsymbol{z} = g_s c \boldsymbol{z}. \tag{2.3}$$

According to the Larmor relation (2.1), all nuclei of a given species in the plane Π_s have the same resonance frequency given by

$$\nu_s = \frac{\gamma}{2\pi}|\boldsymbol{B_0} + \boldsymbol{G_s}| = \frac{\gamma}{2\pi}(B_0 + g_s c). \tag{2.4}$$

Moreover, nuclei out of the plane Π_s have a Larmor frequency that differs from ν_s. Therefore if the RF pulse $\boldsymbol{B_1}$ is applied with a frequency ν_1 tuned to ν_s, then only the nuclei belonging to the plane Π_s will resonate.

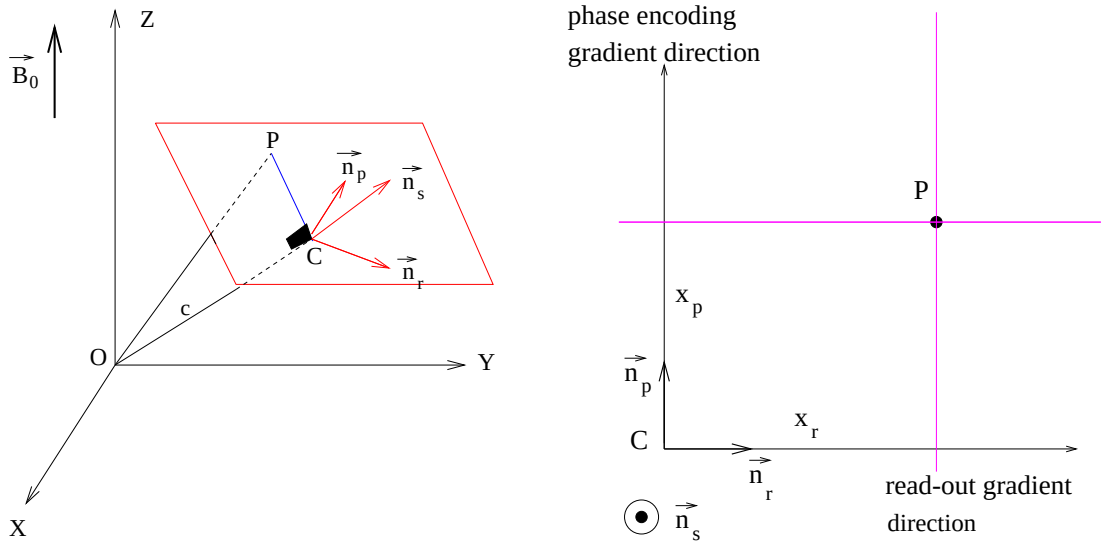

Figure 1: Selection of a slice of the sample.

2.3 Signal encoding in the slice plane

Let $\boldsymbol{n_r}$ and $\boldsymbol{n_p}$ be two orthogonal unit vectors in the plane Π_s. Let (x_r, x_p) denote the coordinates of a point $P \in \Pi_s$ in the coordinate system $(C, \boldsymbol{n_r}, \boldsymbol{n_p})$, see Figure 1. In order to get a signal that contains information on the variations of the nucleus density in the plane Π_s two other gradients are used. *The read-out gradient* $\boldsymbol{G_r}$ is switched on while the signal is collected. The gradient direction is $\boldsymbol{n_r}$ and $\boldsymbol{G_r}$ is expressed as

$$\boldsymbol{G_r}(P) = g_r(\boldsymbol{OP} \cdot \boldsymbol{n_r})\boldsymbol{z} = g_r(\boldsymbol{CP} \cdot \boldsymbol{n_r})\boldsymbol{z} = g_r x_r \boldsymbol{z}. \tag{2.5}$$

Thus the frequency of the MRI signal given by the Larmor relation (2.1) is

$$\nu = \frac{\gamma}{2\pi}|\boldsymbol{B_o} + \boldsymbol{G_r}| = \frac{\gamma}{2\pi}(B_0 + g_r x_r). \tag{2.6}$$

A similar relation between the phase of the signal and the coordinate x_p is obtained by using a third gradient, *the phase-encoding gradient* $\boldsymbol{G_p}$. The gradient direction is $\boldsymbol{n_p}$ and $\boldsymbol{G_p}$ is expressed as

$$\boldsymbol{G_p}(P) = g_p(\boldsymbol{OP} \cdot \boldsymbol{n_p})\boldsymbol{z} = g_p(\boldsymbol{CP} \cdot \boldsymbol{n_p})\boldsymbol{z} = g_p x_p \boldsymbol{z}. \tag{2.7}$$

The phase-encoding gradient is switched on for a brief period T_p before the signal is collected. The phase of the signal given by the Larmor relation (2.1) is

$$\phi = 2\pi\nu_L(P)T_p = \gamma|\boldsymbol{B_o} + \boldsymbol{G_p}|T_p = \gamma(B_0 + g_p x_p)T_p. \tag{2.8}$$

Thus there exist simple relations between the frequency and the phase of the signal in one hand and the coordinates (x_r, x_p) of a point P in the plane Π_s on the other hand. This *phase and frequency spatial encoding* will enable, through a Fourier transform of the signal, to obtain an image of the slice Π_s. Note that in both relations (2.6) and (2.8), frequency and phase origins can be chosen so that the constant term arising from B_0 vanishes.

2.4 Fourier Transform of the signal

In an ideal MRI experiment ignoring relaxation effects, the MRI signal is sinusoidal with a frequency given by (2.6) and a phase given by (2.8). It has the representation

$$S(t_r, g_p) = \int_{\mathbb{R}^2} \rho(x_r, x_p) \ \exp\left(i\,\gamma(g_r x_r t_r + g_p x_p T_p)\right) \, \mathrm{d}x_r \mathrm{d}x_p, \tag{2.9}$$

where the function ρ is the nucleus density of the species in the slice Π_s, see [Callaghan, 1993] or [Morris, 1982].

To extract an expression for the density we write a Fourier transform of the signal, called 2D-FT in the MRI terminology. We introduce the change of variables defined by the mapping $\psi : \mathbb{R}^2 \longrightarrow \mathbb{R}^2$

$$\psi(x_r, x_p) \equiv (\tau_1, \tau_2) = (-\frac{\gamma}{2\pi} g_r x_r, -\frac{\gamma}{2\pi} T_p x_p). \tag{2.10}$$

We denote by J the jacobian of the inverse mapping; J is given by $J = (\gamma\!\!\!^{-}{}^2 T_p g_r)^{-1}$ where $\gamma\!\!\!^{-} = \gamma/2\pi$. With this change of variables, the integral in (2.9) reads

$$S(t_r, g_p) = \int_{\mathbb{R}^2} A(\tau_1, \tau_2) \ \exp(-2\pi i(\tau_1 t_r + \tau_2 g_p)) \, \mathrm{d}\tau_1 \mathrm{d}\tau_2 \tag{2.11}$$

where $A(\tau_1, \tau_2) = \rho(\psi^{-1}(\tau_1, \tau_2))J$. Then (2.11) is the inverse Fourier transform of A. Let $I(\tau_1, \tau_2)$ denote the intensity of the point (τ_1, τ_2) of the image (usually called the image pixel). Then from (2.11) we get by taking the Fourier transform

$$I(\tau_1, \tau_2) = \mathcal{F}[S(t_r, g_p)] = A(\tau_1, \tau_2) = \frac{1}{\gamma\!\!\!^{-}{}^2 T_p g_r} \rho(-\frac{\tau_1}{\gamma\!\!\!^{-} g_r}, -\frac{\tau_2}{\gamma\!\!\!^{-} T_p}). \tag{2.12}$$

Therefore, the two dimensional transform of the collected signal leads to a representation of the density ρ in the plane Π_s. The linear mapping (2.10) can be seen as a scaling between the sample and the image. Note that in practice constant time intervals T_p for the phase encoding are used, the phase variation is achieved through the use of variable phase encoding gradient intensity g_p, see [Morris, 1982] p. 164. The MRI signal can be obtained in practice only for a finite number of values of g_p, each signal being sampled in time in a finite number of points. A discrete Fourier transform is performed to get the image.

3 Theoretical approach of artifacts in MRI

So far we have introduced the techniques of the imaging process. Our goal now is to study in which way magnetic field inhomogeneities give rise to image distortions. This will provide a theoretical basis for the understanding of the observed phenomena as well as a model for the numerical simulation of magnetic susceptibility artifacts.

3.1 Slice selection process disturbances

We establish now the effects of a magnetic field inhomogeneity $\boldsymbol{B}'$ on the slice selection process as described in Section 2.2. During the slice selection process the total magnetic field is given by

$$\boldsymbol{B}(P) = \boldsymbol{B_0} + \boldsymbol{G_s}(P) + \boldsymbol{B}'(P). \tag{3.1}$$

We assume that the magnetic field inhomogeneities are much weaker than the field $\boldsymbol{B_0}$ and we make the following approximation

$$B(P) \approx B_0 + G_s(P) + B'_z(P), \tag{3.2}$$

where B'_z represents the component of the field inhomogeneities along the z direction of the laboratory coordinate system. Hence the Larmor frequency ν_L given by (2.1) is approximated by

$$\nu_L(P) = \frac{\gamma}{2\pi}(B_0 + G_s(P) + B'_z(P)). \tag{3.3}$$

In order to select the plane Π_s the RF pulse $\boldsymbol{B_1}$ is switched on at a frequency ν_1 given by (2.4),

$$\nu_1 = \frac{\gamma}{2\pi}(B_0 + g_s c). \tag{3.4}$$

Nuclei in resonance are those for which the Larmor frequency ν_L is equal to the frequency ν_1. From both equalities (3.3) and (3.4) one deduces that they are not located in the plane Π_s anymore but in the set of points P satisfying

$$G_s(P) + B'_z(P) = g_s c. \tag{3.5}$$

Let us develop this last relation. We denote by (x, y, z) the coordinates of P in the laboratory coordinate system and by (n_1, n_2, n_3) the components of the vector $\boldsymbol{n_s}$. Let $c'(P) = \boldsymbol{OP} \cdot \boldsymbol{n_s} = n_1 x + n_2 y + n_3 z$. According to the equation (2.2) we have

$$G_s(P) = g_s c'(P) = g_s(n_1 x + n_2 y + n_3 z). \tag{3.6}$$

Equation (3.5) can therefore be written as

$$n_1 x + n_2 y + n_3 z + \frac{B'_z(x, y, z)}{g_s} = c. \tag{3.7}$$

It is useful to write Equation (3.7) in the coordinate system $\mathcal{R}_c = (C, \boldsymbol{n_r}, \boldsymbol{n_p}, \boldsymbol{n_s})$. We have

$$x_s + \frac{B'_z(x_r, x_p, x_s)}{g_s} = 0, \tag{3.8}$$

where (x_r, x_p, x_s) denotes the coordinates of P in $\mathcal{R}_c$. Thus magnetic inhomogeneities prevent the selection of a perfectly planar slice Π_s. Instead a warped surface given by the equation (3.7) or (3.8) is selected.

3.2 Signal encoding disturbances

We suppose that the magnetic field inhomogeneity $\boldsymbol{B'}$ also exists when the signal is recorded. Then the static magnetic field is $\boldsymbol{B}(P) = \boldsymbol{B_0} + \boldsymbol{G_r}(P) + \boldsymbol{B'}(P)$. As before we assume that the approximation $B(P) \approx B_0 + G_r(P) + B'_z(P)$ holds. The frequency of the signal is not given by (2.6) anymore. According to the Larmor relation (2.1) we have

$$\nu = \frac{\gamma}{2\pi}B(P) = \frac{\gamma}{2\pi}(B_0 + g_r x_r + B'_z(x_r, x_p, x_s)). \tag{3.9}$$

In a similar way the phase of the MRI signal becomes

$$\phi(P) = 2\pi\nu_L(P)T_p = \gamma B(P)T_p = \gamma(B_0 + g_p x_p + B'_z(x_r, x_p, x_s))T_p. \tag{3.10}$$

The effect of the phase shift in (3.10) depends on the MRI sequence, see [Morris, 1982] for a complete description. For the Spin-Echo sequence, the phase shift due to magnetic field inhomogeneities can be compensated when the signal is collected, contrarily for the Gradient-Echo sequence it is not. Since we want to handle the two cases, we introduce a parameter k_d with value 0 when the phase shift can be ignored and with value 1 in the other case. Moreover we need to take into account that the perturbation exists not only during the time T_p when the phase encoding gradient is turned on, but since the sequence inception, that is for a time T_E. Therefore the phase of the signal is given by

$$\phi(P) = \gamma(B_0 + g_p x_p T_p + k_d B'_z(x_r, x_p, x_s)T_E). \tag{3.11}$$

So to take into account the effects of field inhomogeneities represented by $B'(x_r, x_p, x_s)$, we will replace the equations (2.6) and (2.8) for the frequency and the phase by the (3.9) and (3.11) ones. From now on the frequency and phase origins are chosen so that the constant term arising from $\boldsymbol{B_0}$ vanishes in (3.9) and (3.11).

3.3 Fourier transform of the perturbed signal

We want to image now a slice of a sample in the presence of a magnetic field perturbation $\boldsymbol{B'}$. The phase and the frequency of the signal, as well as the location of the excited nuclei are modified in a way given by the relations (3.11), (3.9), and (3.8). Accordingly like in (2.9), the MRI signal has the representation

$$\begin{aligned} S(t_r, g_p) &= \int_{\mathbb{R}^2} \rho(x_r, x_p, x_s(x_r, x_p)) \\ &\times \exp\left(i\,\gamma(g_r x_r + B'_z(x_r, x_p, x_s(x_r, x_p)))t_r\right) \\ &\times \exp\left(i\,\gamma(g_p x_p T_p + k_d B'_z(x_r, x_p, x_s(x_r, x_p))T_E)\right)\, \mathrm{d}x_r \mathrm{d}x_p \end{aligned} \tag{3.12}$$

where x_s is a solution of the nonlinear equation

$$x_s + \frac{B'_z(x_r, x_p, x_s)}{g_s} = 0. \tag{3.13}$$

For ease of exposition we assume there exists a unique x_s satisfying (3.13), while a detailed exposition would include in (3.12) an additional summation term over the different solutions of (3.13). We will write $\overline{B'_z}(x_r, x_p)$ instead of $B'_z(x_r, x_p, x_s(x_r, x_p))$ and $\overline{\rho}(x_r, x_p)$ instead of $\rho(x_r, x_p, x_s(x_r, x_p))$. We also set $\gamma = \gamma/2\pi$ and carry out a Fourier transform of the signal to simulate the way in which the image is obtained. The function S given in (3.13) doesn't have the required regularity to achieve the Fourier transform in the usual way. We will use the Fourier transform in the sense of distributions.

Let $\mathcal{S}(\mathbb{R}^2)$ be the space of infinitely differentiable functions with all derivatives decreasing rapidly and $\mathcal{S}'(\mathbb{R}^2)$ be its dual space ($\mathcal{S}'(\mathbb{R}^2)$ is the space of tempered distributions). The Fourier transform of S as a distribution is defined by, see [Schwartz, 1961],

$$< \mathcal{F}S, \phi > = < S, \hat{\phi} > \qquad \forall \phi \in \mathcal{S}(\mathbb{R}^2),$$

where $\hat{\phi}$ is the Fourier transform of ϕ in the usual way and $<,>$ the duality product $\mathcal{S}'(\mathbb{R}^2) \times \mathcal{S}(\mathbb{R}^2)$. Let I be the Fourier transform of S. We have for $\phi \in \mathcal{S}(\mathbb{R}^2)$,

$$\begin{aligned} < I, \phi > &= < S, \hat{\phi} > \\ &= \int_{\mathbb{R}^2} S(t_r, g_p)\hat{\phi}(t_r, g_p)\, \mathrm{d}t_r \mathrm{d}g_p \\ &= \int_{\mathbb{R}^2} \Big\{ \int_{\mathbb{R}^2} \overline{\rho}(x_r, x_p) \exp\left(i\,\gamma(g_r x_r + \overline{B_z'}(x_r, x_p))t_r\right) \\ &\times \exp\left(i\,\gamma(g_p x_p T_p + k_d \overline{B_z'}(x_r, x_p)T_E)\right)\, \mathrm{d}x_r \mathrm{d}x_p \Big\}\, \hat{\phi}(t_r, g_p)\, \mathrm{d}t_r \mathrm{d}g_p. \end{aligned} \tag{3.14}$$

By interchanging the order of integration we obtain

$$\begin{aligned} < I, \phi > = & \int_{\mathbb{R}^2} \overline{\rho}(x_r, x_p) \exp\left(i\,\gamma k_d \overline{B_z'}(x_r, x_p)T_E\right) \\ & \times \Big\{ \int_{\mathbb{R}^2} \exp\left(i\,\gamma((g_r x_r + \overline{B_z'}(x_r, x_p))t_r + g_p x_p T_p)\right) \hat{\phi}(t_r, g_p)\, \mathrm{d}t_r \mathrm{d}g_p \Big\}\, \mathrm{d}x_r \mathrm{d}x_p. \end{aligned} \tag{3.15}$$

We set $\widetilde{\rho}(x_r, x_p) = \overline{\rho}(x_r, x_p) \exp\left(i\,\gamma k_d \overline{B_z'}(x_r, x_p)T_E\right)$ and recognize inside the brackets the inverse Fourier transform of the function $\hat{\phi}$ taken in $(-\gamma\,(g_r x_r + \overline{B_z'}(x_r, x_p)), -\gamma\, x_p T_p)$, that is

$$\begin{aligned} & \int_{\mathbb{R}^2} \exp\left(i\,\gamma((g_r x_r + \overline{B_z'}(x_r, x_p))t_r + g_p x_p T_p)\right)\ \hat{\phi}(t_r, g_p)\, \mathrm{d}t_r \mathrm{d}g_p \\ & \quad = \phi(-\gamma\,(g_r x_r + \overline{B_z'}(x_r, x_p)), -\gamma\, x_p T_p). \end{aligned} \tag{3.16}$$

Thus the Fourier transform I of S is given by

$$< I, \phi > = \int_{\mathbb{R}^2} \widetilde{\rho}(x_r, x_p)\phi(-\gamma\,(g_r x_r + \overline{B_z'}(x_r, x_p)), -\gamma\, x_p T_p)\, \mathrm{d}x_r \mathrm{d}x_p. \tag{3.17}$$

Let us consider the change of variables defined by

$$\psi : (x_r, x_p) \in \mathbb{R}^2 \longmapsto (\tau_1(x_r, x_p), \tau_2(x_r, x_p)) \in \mathbb{R}^2$$

where

$$\left\{ \begin{array}{lcl} \tau_1(x_r, x_p) & = & -\gamma\,(g_r x_r + \overline{B_z'}(x_r, x_p)), \\ \tau_2(x_r, x_p) & = & -\gamma\, x_p T_p. \end{array} \right. \tag{3.18}$$

The function ψ is not necessarily bijective because of the term $B_z'(x_r, x_p, x_r(x_r, x_p))$ arising from the field inhomogeneities. Nevertheless since $\boldsymbol{B}$ is piecewise regular, one can find a covering of $\cup_{j=1}^{N} \overline{U_j} = \mathbb{R}^2$ made up of a finite number N of open sets U_j such that, $\forall j = 1, \ldots, N$, $\psi : (x_r, x_p) \in U_j \longmapsto (\tau_1(x_r, x_p), \tau_2(x_r, x_p)) \in V_j$ is bijective. Let J_j be the jacobian of the inverse of ψ_j, the restriction of ψ in U_j

$$J_j = \frac{1}{\gamma^2 T_p \left(g_r + \dfrac{\partial}{\partial x_r} \overline{B_z'}(x_r, x_p) \right)}. \tag{3.19}$$

We have

$$\begin{aligned} < I, \phi > &= \int_{\mathbb{R}^2} \Big\{ \sum_{j=1}^{N} \widetilde{\rho}(x_r, x_p)\phi(-\gamma\,(g_r x_r + \overline{B_z'}(x_r, x_p)), -\gamma\, T_p x_p)\aleph_{U_j} \Big\}\, \mathrm{d}x_r \mathrm{d}x_p \\ &= \sum_{j=1}^{N} \int_{U_j} \widetilde{\rho}(x_r, x_p)\phi(-\gamma\,(g_r x_r + \overline{B_z'}(x_r, x_p)), -\gamma\, T_p x_p)\, \mathrm{d}x_r \mathrm{d}x_p, \end{aligned} \tag{3.20}$$

where $\aleph_{U_j}(x_r, x_p) = 1$ if $(x_r, x_p) \in U_j$ and $\aleph_{U_j}(x_r, x_p) = 0$ if $(x_r, x_p) \notin U_j$. The use of the change of variables (3.18) in (3.20) gives

$$\begin{aligned} < I, \phi > &= \sum_{j=1}^{N} \int_{V_j} \phi(\tau_1, \tau_2)\ \widetilde{\rho}(\psi_j^{-1}(\tau_1, \tau_2)) J_j(\tau_1, \tau_2)\, \mathrm{d}\tau_1 \mathrm{d}\tau_2 \\ &= \int_{\mathbb{R}^2} \Big\{ \sum_{j=1}^{N} \phi(\tau_1, \tau_2)\ \widetilde{\rho}(\psi_j^{-1}(\tau_1, \tau_2)) J_j(\tau_1, \tau_2)\ \aleph_{V_j} \Big\}\, \mathrm{d}\tau_1 \mathrm{d}\tau_2 \\ &= < \sum_{j=1}^{N} (\widetilde{\rho} \circ \psi_j^{-1}) J_j\ \aleph_{V_j}, \phi > . \end{aligned} \tag{3.21}$$

Henceforth we have

$$I(\tau_1, \tau_2) = \sum_{j=1}^{N} \widetilde{\rho}(\psi_j^{-1}(\tau_1, \tau_2)) J_j(\tau_1, \tau_2) \aleph_{V_j}(\tau_1, \tau_2). \tag{3.22}$$

Eventually from the expression (3.22) with the change of variables (3.18) we deduce that the intensity of the image pixel (τ_1, τ_2) is given by

$$\begin{aligned} I(\tau_1, \tau_2) = & \sum_{\substack{(x_r, x_p, x_s) \\ \text{solution of (3.24)}}} \rho(x_r, x_p, x_s) \exp\left(i\, \gamma k_d B_z'(x_r, x_p, x_s) T_E\right) \\ & \times \frac{1}{|1 + \dfrac{1}{g_r} \dfrac{\partial}{\partial x_r} B_z'(x_r, x_p, x_s)|}, \end{aligned} \tag{3.23}$$

where

$$\left\{ \begin{array}{lcl} x_r + \dfrac{B_z'(x_r, x_p, x_s)}{g_r} & = & \tau_1, \\ x_p & = & \tau_2, \\ x_s + \dfrac{B_z'(x_r, x_p, x_s)}{g_s} & = & 0. \end{array} \right. \tag{3.24}$$

In (3.23) we have included the case where (3.13) has several solutions. Moreover, the constant coefficients γ in (3.24) and $1/\gamma^2 T_p g_r$ in (3.23) are omitted. They can be interpreted as scaling coefficients.

3.4 The pulse bandwidth

For ease of exposition we have assumed so far that the RF pulse $\boldsymbol{B_1}$ is emitted at a single frequency ν_1. In practice the RF pulse contains a range of frequencies (or bandwidth) $\nu_1 \pm \frac{1}{2}\Delta\nu_1$. Thus all the nuclei whose Larmor frequency is equal to one of the frequencies in the bandwidth resonate. Consequently a layer of thickness e_s around the plane Π_s is imaged. One can check that the slice width is given by

$$e_s = \frac{2\pi}{\gamma} \frac{\Delta\nu_1}{g_s}. \tag{3.25}$$

Therefore in order to take into account the pulse bandwidth an additional summation term over the slice thickness e_s is to be introduced. The signal is expressed as

$$\begin{aligned} S(t_l, g_p) &= \int_{-\frac{1}{2}e_s}^{\frac{1}{2}e_s} \int_{\mathbb{R}^2} \rho(x_r, x_p, x_s(x_r, x_p, \zeta)) \\ &\quad \times \exp\left(i\,\gamma(g_r x_r + B'_z(x_r, x_p, x_s(x_r, x_p, \zeta)))t_r\right) \\ &\quad \times \exp\left(i\,\gamma(g_p x_p T_p + k_d B'_z(x_r, x_p, x_s(x_r, x_p, \zeta))T_E)\right)\, \mathrm{d}x_r \mathrm{d}x_p \mathrm{d}\zeta \end{aligned} \tag{3.26}$$

where x_s satisfies

$$x_s + \frac{B'_z(x_r, x_p, x_s)}{g_s} = \zeta \qquad \text{with } \zeta \in [-\tfrac{1}{2}e_s, \tfrac{1}{2}e_s]. \tag{3.27}$$

Our development for the Fourier transform of the signal remains valid. One should read $\overline{I}(x_r, x_p) = I(x_r, x_p, x_s(x_r, x_p, \zeta))$ and $\overline{B'_z}(x_r, x_p) = B'_z(x_r, x_p, x_s(x_r, x_p, \zeta))$, and carry an integration over the variable $\zeta \in [-\frac{1}{2}e_s, \frac{1}{2}e_s]$. Expressions (3.23) and (3.24) become

$$\begin{aligned} I(\tau_1, \tau_2) &= \int_{-\frac{1}{2}e_s}^{\frac{1}{2}e_s} \sum_{\substack{(x_r, x_p, x_s) \\ \text{solution of (3.29)}}} \rho(x_r, x_p, x_s) \exp\left(i\,\gamma k_d B'_z(x_r, x_p, x_s)T_E\right) \\ &\times \frac{1}{|1 + \dfrac{1}{g_r}\dfrac{\partial}{\partial x_r} B'_z(x_r, x_p, x_s)|} \mathrm{d}\zeta, \end{aligned} \tag{3.28}$$

where

$$\begin{cases} x_r + \dfrac{B'_z(x_r, x_p, x_s)}{g_r} = \tau_1, \\ x_p = \tau_2, \\ x_s + \dfrac{B'_z(x_r, x_p, x_s)}{g_s} = \zeta. \end{cases} \tag{3.29}$$

4 Analysis of magnetic susceptibility artifacts

With the relations (3.28) and (3.29) we have formulae to get the intensity of the image pixel (τ_1, τ_2). They will be used first to study from a theoretical point of view the effects of magnetic inhomogeneities on MRI images. We will see that these two mathematical relations enable to find again the well known effects of magnetic perturbations on an MRI experiment as described in [Ludeke *et al*, 1985], [Ericsson *et al*, 1988] or [Schenck, 1996] for instance. These relations also enable to accurately quantify the various distortions giving rise to the artifact. In the next section relations (3.28) and (3.29) will be used to develop numerical methods to compute artifacts.

4.1 Geometric distortions

In Section 3.1 we saw that magnetic field inhomogeneities prevent the selection of the plane Π_s of equation $x_s = 0$. Instead a surface Σ_s with equation

$$x_s + \frac{B'_z(x_r, x_p, x_s)}{g_s} = 0 \tag{4.1}$$

is selected, we recall that (x_r, x_p, x_s) are in the coordinate system $(C, \boldsymbol{n_r}, \boldsymbol{n_p}, \boldsymbol{n_s})$. Thus the actual position of the points in the sample is shifted from the plane Π_s by a quantity

$$\Delta c(P) = \frac{B'_z(P)}{g_s} \tag{4.2}$$

in the direction $\boldsymbol{n_s}$ of the slice selection gradient. Consequently a non planar surface with a varying thickness is being imaged instead of the desired plane Π_s. We can observe that the slice selection disturbances could be reduced by increasing the intensity g_s of the slice-selection gradient. Unfortunately this intensity is limited by technical constraints.

The first two equations in (3.29) express the disturbances of the phase and frequency spatial encoding process. In the absence of magnetic field inhomogeneities, a point $P = (x_r, x_p, 0)$ belonging to the plane Π_s is depicted in the image at the position $(\tau_1 = x_r, \tau_2 = x_p)$. In the presence of a magnetic field $\boldsymbol{B'}$ a point $P = (x_r, x_p, x_c)$ belonging to the surface Σ_s is depicted at

$$(\tau_1 = x_r + \frac{B'_z(x_r, x_p, x_s)}{g_r}, \tau_2 = x_p). \tag{4.3}$$

Thus field's inhomogeneities are liable for distortions in the read-out gradient direction $\boldsymbol{n_r}$ but do not affect the image in the phase encoding direction $\boldsymbol{n_p}$, this is one of the well known advantages of the 2D-FT image reconstruction method, see [Morris, 1982], p.165.

In addition to that, due to the magnetic field inhomogeneities the distance between two points in the sample is not preserved in the image. Let $P = (x_r, x_p, x_s)$ and $P' = (x'_r, x'_p, x_s)$ be two points in Σ_s. Let $\delta_r = x'_r - x_r$ and $\delta_p = x'_p - x_p$. The distance in the sample between the two points is $\delta = \sqrt{\delta_r^2 + \delta_p^2}$. If (τ_1, τ_2) and (τ'_1, τ'_2) are the two corresponding image pixels, then we have from the system (3.29)

$$\left\{ \begin{array}{rcl} \tau'_1 & = & \tau_1 + \delta_r + \frac{1}{g_r}\big(B'_z(P') - B'_z(P)\big), \\ \tau'_2 & = & \tau_2 + \delta_p. \end{array} \right. \tag{4.4}$$

The distance between the two pixels in the image is

$$\Delta = \sqrt{\Big(\delta_r + \frac{1}{g_r}\big(B'_z(P') - B'_z(P)\big)\Big)^2 + \delta_p^2}. \tag{4.5}$$

Thus in the presence of magnetic field inhomogeneities the actual distances are not preserved in the image. Moreover if the magnetic field $\boldsymbol{B'}$ varies abruptly then two points that are close to each other in the sample may appear far from each other in the image. Such a steep variation happens for two points in two media with strongly different magnetic properties, for instance a metallic implant and a biological tissue. It is well known, see [Jackson, 1975], that the magnetic field has a discontinuity at the interface between the two media which is proportional to the variation of the magnetic susceptibility χ_m.

In order to illustrate the image distortions we will consider the special case of a metallic ball (the implant) embedded in a homogeneous diamagnetic substance (the biological tissues) and submitted to the magnetic flux density $\boldsymbol{B_0}$. The ball radius is 1 cm and its magnetic susceptibility is $\chi_m = 10^{-3}$. The magnetic flux density strength is $B_0 = 1$ Tesla and the intensity of the gradients is $g = 10^{-2}$ Tesla per meter. The magnetic field inhomogeneities are due to the magnetic field $\boldsymbol{B'}$ induced by the ball, see [Jackson, 1975] for its analytical expression. The slice Π_s to be imaged is parallel to $\boldsymbol{B_0}$ and intersect the ball through its center, see Figure 2. The slice is 3 cm long and 3 cm wide. Figure 3 shows the surface Σ_s with equation given in (4.1) and the geometric distortions given in (4.3).

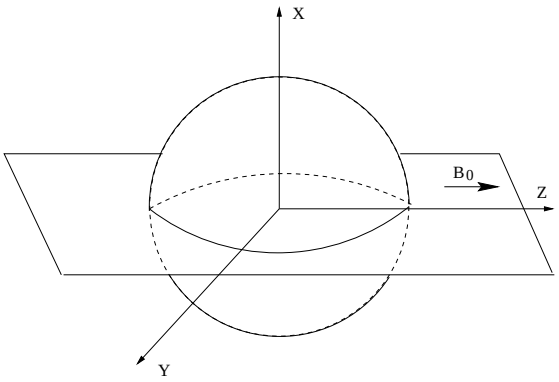

Figure 2: Slice to be imaged.

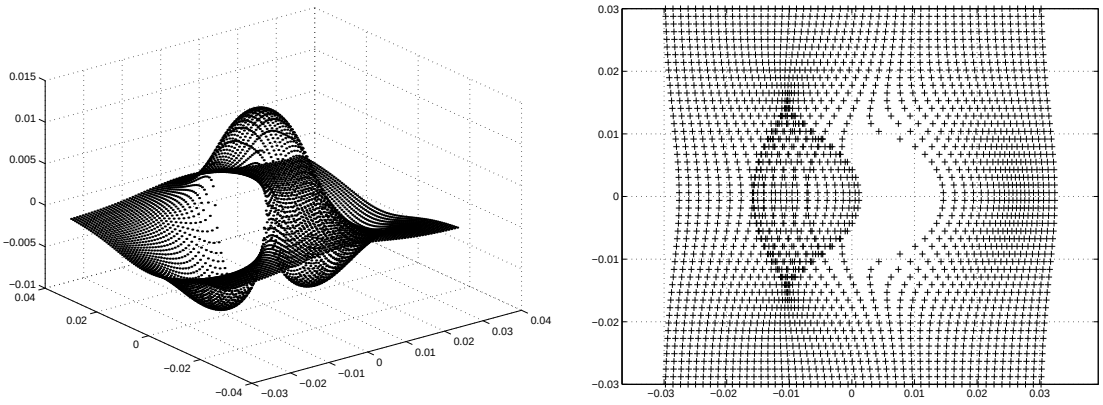

Figure 3: (a) Distortion of the slice to be imaged (in meter) and (b) geometric distortions.

4.2 Intensity distortions

Intensity distortions may have three different origins.

If there exist several solutions (x_r, x_p, x_s) to the equations (3.29) for a given right-hand side (τ_1, τ_2, ζ), then several points of the sample are associated to the same image pixel. Contrarily if the system (3.29) has no solution, no point of the sample corresponds to the given pixel. The result is an intensity enhancement in the first case and a cancellation in the second case.

The intensity distortions are due as well to the variations of the field $\boldsymbol{B}'$ (in fact its component B'_z) in the read-out gradient direction. This distortion is given in (3.28) by the term

$$D = \frac{1}{|1 + \frac{1}{g_r}\frac{\partial}{\partial x_r} B'_z(x_r, x_p, x_s)|}. \tag{4.6}$$

If B'_z increases in the direction of the read-out gradient then $\frac{\partial}{\partial x_r} B'_z(x_r, x_p, x_s) > 0$ and the intensity decreases, $D < 1$. On the contrary, if B'_z decreases then $\frac{\partial}{\partial x_r} B'_z(x_r, x_p, x_s) < 0$ and the intensity raises, $D > 1$.

Finally the term $\exp\left(i\,\gamma k_d B'_z(x_r, x_p, x_s(x_r, x_p, \zeta))T_E\right)$ in (3.28) expresses that for some imaging sequences (such as the Gradient-Echo sequence), magnetic inhomogeneities give rise to intensity distortions due to additional phase shifts.

5 Algorithms and numerical simulation

To compute magnetic susceptibility artifacts now it suffices to evaluate the integral in (3.28), once the magnetic perturbation fields $\boldsymbol{B'}$ is known.

5.1 A first algorithm

We wish to numerically compute the image intensity I in (3.28) on a given pixel (τ_1, τ_2). The integral is evaluated with a gaussian quadrature rule. We have

$$I(\tau_1, \tau_2) = \int_{-\frac{1}{2}e_s}^{\frac{1}{2}e_s} A(\tau_1, \tau_2, \zeta)\, \mathrm{d}\zeta \approx \frac{e_s}{2} \sum_{k=1}^{\mu_d} \omega_k A(\tau_1, \tau_2, u_k) \tag{5.1}$$

where the $\omega_k \in \mathbb{R}$ are the quadrature weights and $u_k \in [-1, 1]$ are the quadrature nodes.

The main task is then to determine the point(s) (x_r, x_p, x_c) in the sample that are represented in (τ_1, τ_2), that is to solve the system (3.29). This system can be written, by combining the first and third equations, as follows

$$\left\{ \begin{array}{lcll} x_r & + & \dfrac{g_s}{g_r}(\zeta - x_s) & = \tau_1, \\ x_p & & & = \tau_2, \\ x_s & + & \dfrac{B'_z(x_r, x_p, x_s)}{g_s} & = \zeta, \text{ where } \zeta \in [-\frac{1}{2}e_s, \frac{1}{2}e_s]. \end{array} \right. \tag{5.2}$$

Thus we have to solve the following non linear problem: find $x_s \in \mathbb{R}$ solution to

$$x_s + \frac{B'_z(x_r, x_p, x_s)}{g_s} = \zeta \tag{5.3}$$

where

$$\left\{ \begin{array}{lcl} x_r & = & \tau_1 + \dfrac{g_s}{g_r}(x_s - \zeta), \\ x_p & = & \tau_2, \\ \zeta & \in & [-\frac{1}{2}e_s, \frac{1}{2}e_s]. \end{array} \right. \tag{5.4}$$

Let $F : \mathbb{R} \longrightarrow \mathbb{R}$ be defined by

$$x_s \longmapsto F(x_s) = (x_s - \zeta) + \frac{1}{g_s} B'_z(\tau_1 + \frac{g_s}{g_r}(x_s - \zeta), \tau_2, x_s), \tag{5.5}$$

where the parameters $g_s, g_r, g_p, \tau_1, \tau_2$ and ζ are fixed. Solving (5.3) and (5.4) is equivalent to find the zeros x_s of F. The values of x_r and x_p are then obtained by (5.4).

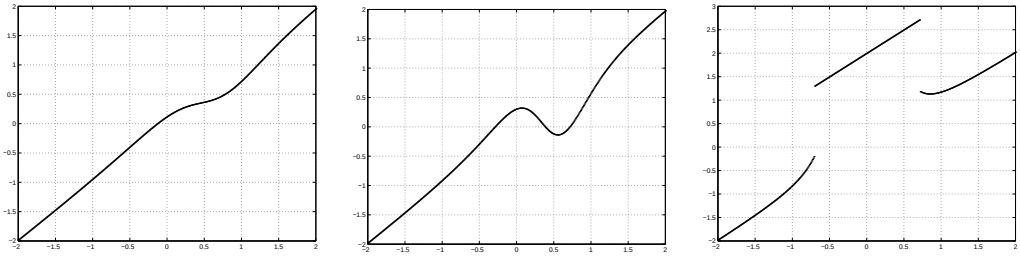

Figure 4: Graph of the function F in the case of the ball. The parameters τ_1, τ_2, and ζ correspond to a point far from the ball (left), close to the ball (middle) and inside the ball (right).

We derive the following formal algorithm

Algorithm 1

For each pixel (τ_1, τ_2) **do**
  For $k = 1, \ldots, \mu_d$ **do**
    For each x_s solution of $F(x_s) = 0$ **do**
      Set $x_r = \tau_1 + \frac{g_s}{g_r}(x_s - \zeta)$ and $x_p = \tau_2$
      Compute $\rho(x_r, x_p, x_s)$, $B'_z(x_r, x_p, x_s)$ and $\dfrac{\partial}{\partial x_r} B'_z(x_r, x_p, x_s)$
      Set

$$I(\tau_1, \tau_2) = I(\tau_1, \tau_2) + \rho(x_r, x_p, x_s) \frac{\exp\left(i\,\gamma k_d B'_z(x_r, x_p, x_s) T_E\right)}{|1 + \frac{1}{g_r}\frac{\partial}{\partial x_r} B'_z(x_r, x_p, x_s)|}$$

    End do
  End do
End do

We have implemented Algorithm 1 in the case of a ball where the analytical expression for F is known, see the example at the end of Subsection 4.1. One observes that the function F given in (5.5) is not necessarily continuous (this is due to the jump of the magnetic field $\boldsymbol{B'}$ across the ball boundary) and the number of its zeros depends on the values of the parameters τ_1, τ_2, and ζ. In Figure 4 we have depicted the graph of F for several values of τ_1, τ_2, and ζ in the case of the ball discussed in Subsection 4.1. We can observe that the number of zeros varies from 0 to 3. The behavior of F is therefore liable to change depending on the experimental parameters $g_s, g_r, g_p, \tau_1, \tau_2$ and ζ. In practise, for metallic implants of general shape there is no analytical expression for the magnetic field $\boldsymbol{B'}$ and therefore F can only be computed pointwise. Therefore no efficient numerical code based on Algorithm 1 can be elaborated.

5.2 An alternative approach

It is possible to overcome the difficulty of finding the zeros of F by working in a different way. The idea is to go over the sample and to test whether the nuclei at a given point (x_r, x_p, x_s) resonate or not. In that case we compute the pixel where this point is depicted in the image and we increase the pixel intensity by the corresponding value. This approach

is applied in the following algorithm.

Algorithm 2

For $(x_r, x_p, x_s) \in \mathbb{R}^3$ **do**:
Compute (τ_1, τ_2, ζ) such that

$$\begin{cases} \tau_1 &= x_r &+ \dfrac{B'_z(x_r, x_p, x_s)}{g_r} \\ \tau_2 &= x_p & \\ \zeta &= x_s &+ \dfrac{B'_z(x_r, x_p, x_s)}{g_s} \end{cases}$$

If $\zeta \in [-\frac{1}{2}e_s, \frac{1}{2}e_s]$ and (τ_1, τ_2) belongs to the image **then**

$$I(\tau_1, \tau_2) = I(\tau_1, \tau_2) + \rho(x_r, x_p, x_s) \frac{\exp\left(i\,\gamma k_d B'_z(x_r, x_p, x_s) T_E\right)}{|1 + \frac{1}{g_r}\frac{\partial}{\partial x_r} B'_z(x_r, x_p, x_s)|}$$

End if
End do

In practice, a large volume around the object is chosen. This volume is subdivided into small cubes. Inside each cube a point (x_r, x_p, x_s) is chosen. Previous works on numerical simulation of susceptibility artifacts were based on this approach, see [Ericsson *et al*, 1988], [Bakker, 1993] for instance. The main disadvantage of this approach is that it requires computations for a large number of points. Now most of these points would not be depicted in the image. Fortunately it is possible to limit the area around the object in which the points depicted in the image lie. We have implemented Algorithm 2 to simulate MRI artifacts induced by metallic implants of general shape, see [Balac, 1997].

5.3 Computation of the magnetic field perturbations

Most of the previously presented computer simulations regarding magnetic susceptibility artifacts have only consider the case when an analytical expression for the magnetic field perturbations is known. It means that simulation were limited to simple geometrical objects such as sphere, cylinder or ellipsoid, see [Ludeke *et al*, 1985], [Ericsson *et al*, 1988], [Bakker, 1993] for instance. In general, a precise calculation of the magnetic field involves a boundary value problem with partial differential equations (PDE) derived from Maxwell's equations and requires the use of PDE approximation schemes. Among the classical numerical methods are the finite element method (FEM) and the finite difference method (FDM). These methods are used by [Bhagwandien *et al*, 1994] and [Li *et al*, 1995] to investigate the distortion of the static magnetic field in 2D anatomical models.

As serious limitation of the FDM stands in the calculation of the boundary conditions on non-planar boundaries. Furthermore, when applying the FDM or the FEM to electromagnetic field problems the exterior domain has to be truncated and an approximation of the behavior of the field at infinity has to be enforced on an artificial boundary.

In [Balac & Caloz, 1996] and [Balac & Caloz, 1998] we have developed a method to compute the magnetic field induced by paramagnetic implants of very general shape that avoid the limitations of the FDM or the FEM for this particular problem. Our approach is rather similar to the one used in the boundary element method (BEM) and is based

on a surface integral representation formula for the magnetic flux density. For short, our method consists in writing the problem into an integral form over the boundary of the implant and chopping the boundary into pieces on each of which the integral is numerically computed. It is able to deal with objects of any shape provided that a mesh of the object boundary is available. This requirement is not at all restricting since mesh generation tools are widely used in computer assisted design (CAD). The advantages of our method compared to the FEM or to the FDM are numerous. First, the computation only turns on the object boundary so that the discretization space is reduced from 3D to 2D. Moreover the behavior at infinity is always exactly satisfied. Last, for 3D problems the FEM and the FDM lead to large linear systems to be solved, whereas in the propound method the solution is obtained pointwise by evaluating a surface integral.

5.4 Numerical results

In the case of the metallic ball of radius r_0 and magnetic susceptibility χ_m a very efficient way to numerically simulate magnetic susceptibility artifacts is given by Algorithm 1. From the analytical expression of the magnetic field induced by a ball, see [Jackson, 1975], we derive the following expression for F,

$$\begin{aligned} F(x_s) &= (x_s - c) + \frac{\chi_m B_0 r_0^3}{3 g_s} \left(\frac{3\,(\boldsymbol{z}.\boldsymbol{r})^2}{r^5} - \frac{1}{r^3} \right) \quad \text{if } r > r_0, \\ &= (x_s - c) + \frac{2\chi_m B_0}{3 g_s} \qquad\qquad\qquad\qquad\quad \text{if } r < r_0. \end{aligned} \tag{5.6}$$

Multiplying each side of the equation $F(x_s) = 0$ by an appropriate *conjugate quantity* we obtain that the zeros of F are among the roots of a polynomial $P(x_s)$ of degree 12. A Matlab program that uses this approach to simulate artifacts induced by a metallic ball can be obtained from the authors. Figure 5 (a) shows the experimental artifact obtained when an MRI image of the slice depicted in Figure 2 is done. This experimental image has to be compared to the numerically simulated image shown in Figure 5 (b) which is obtained by using our Matlab program.

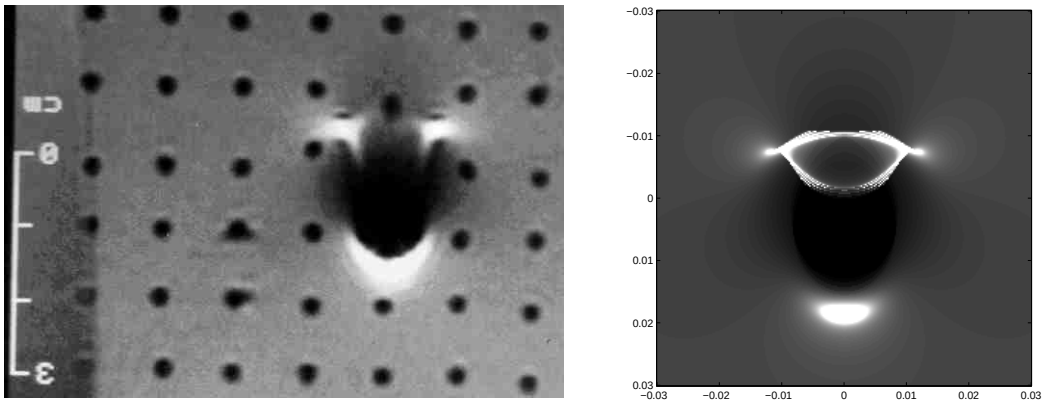

Figure 5: Magnetic susceptibility artifact generated by a metallic ball; (a) experimental image (left) and (b) numerically simulated image (right).

The computational method of the magnetic field perturbation induced by a metallic implant described in section 5.3 is used together with Algorithm 2 to get simulated images of the artifacts generated by objects of general shape. To illustrate the efficiency of the

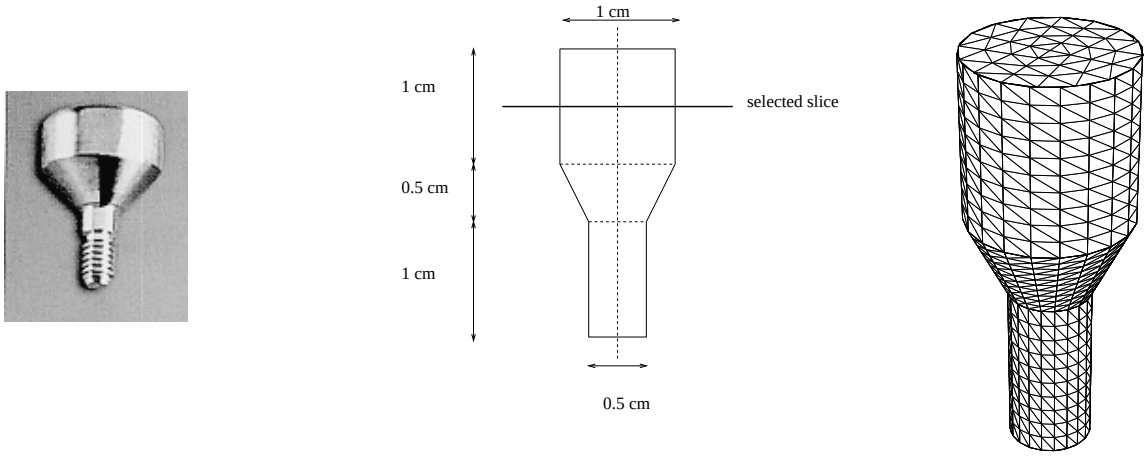

Figure 6: Dental implant chosen to illustrate the effectiveness of the method, position of the slice and mesh (1328 triangles) of the implant boundary used to compute the magnetic field perturbation.

method we present some simulations carried out with a dental implant depicted in Figure 6. This implant has a magnetic susceptibility of 10^{-3} usi and is placed in a 0.5 T magnetic flux density $\boldsymbol{B_0}$. The mesh of the implant boundary used to compute the magnetic field perturbation has 1328 triangles (we have neglected the thread of the screw). The slice depicted in Figure 6, has a side length of 5 cm and is parallel to the magnetic flux density $\boldsymbol{B_0}$. The slice-selection gradient and the read-out gradient strength are 10^{-2} T/m. The slice thickness is 3 mm. Figure 7 shows the isolines for B'_z and the numerically computed artifact. To obtain the corresponding experimental image the implant was placed centrally in a box filled with a diamagnetic substance ($CuSO_4$ at a concentration of 0.6 g/l). The slice was recorded using a Spin-Echo sequence with a repetition time of 490 ms and an echo time of 25 ms.

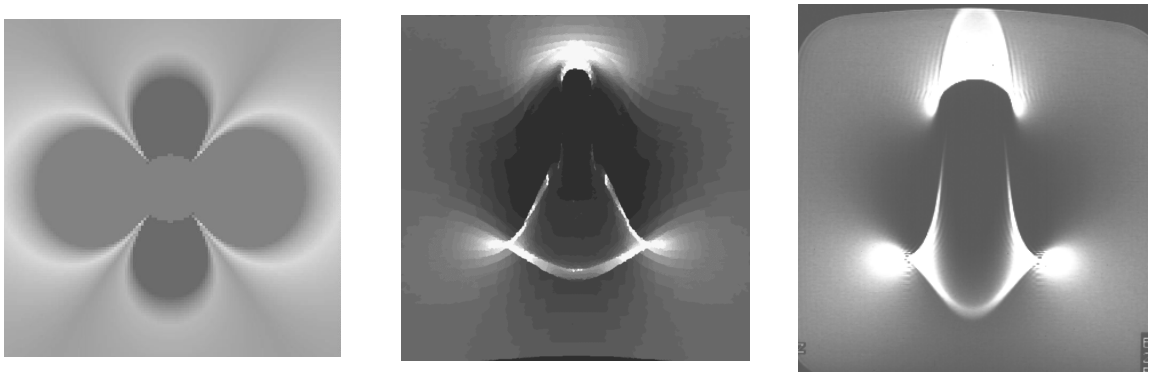

Figure 7: Isolines for B'_z, simulated Spin-Echo image and experimental MR Images (SE 490/25). The frequency encoding gradient direction is left-right, the side length of the figures corresponds to 5 cm actual distance.

6 Conclusion

We have developed and analyzed a mathematical model which represents image distortions in MRI generated by magnetic field inhomogeneities. Algorithms for the numerical simulations are derived. These algorithms are implemented in a software to get simulated images of the magnetic susceptibility artifacts generated by implants of very general shape. The software could be very useful to investigate new medical implants that would not be so sensitive to artifacts, see [Chauvel *et al*, 1996]. Presently many experiments on MRI imagers have to be carried out. In the future we intend to merge our approach with the one presented in [Olsson *et al*, 1995] to simulated images of the magnetic susceptibility artifacts generated by implants of general shape for any MRI pulses sequence. A last step in the mathematical study of MRI susceptibility artifacts would be to propose post processing methods to retrieve the original image.

References

Abele, M. *et al.* (1994) Compensation of field distortion with ferromagnetic material and permanent magnets. *Journal of Applied Physics*, **75**, 6990-6992.

Bakker, C. *et al.* (1993) Susceptibility artifacts in 2DFT spin-echo and gradient-echo imaging, the cylinder model revisited. *Magnetic Resonance Imaging*, **11**, 539-548.

Balac, S. & Caloz, G. (1996) Magnetic susceptibility artifacts in magnetic resonance imaging. Calculation of the magnetic field disturbances. *IEEE Transactions on Magnetics*, **32**, 1645-1648.

Balac, S. (1997) *Artefacts de susceptibilité magnétique en IRM : étude du problème de magnétostatique et simulation numérique.* PhD thesis, Université de Rennes 1, Rennes, France.

Bhagwadien, R. *et al* (1994) Numerical analysis of the magnetic field of arbitrary magnetic susceptibilitry distributions in 3D. *Magnetic Resonance Imaging*, **12**, 101-107.

Callaghan, P.T. (1993) *Principles of Nuclear Magnetic Resonance microscopy.* Clarendon Press.

Chauvel, B. *et al.* (1996) Cancellation of metal-induced MRI artifacts with dual-component paramagnetic and diamagnetic material: mathematical modelization and experimental verification. *Journal of Magnetic Resonance Imaging*, **6**, 936-938.

Davison, M.E. & Grunbaum, F.A. (1973) Tomographic reconstruction with arbitrary directions. *Communications on Pure and Applied Mathematics*, **34**, 77-120.

Erricsson, A. *et al.* (1988) Calculation of MRI artefacts caused by static field disturbances. *Physics in Medicine and Biology*, **33**(10), 1103-1112.

Fache, J. *et al.* (1987) MR Imaging artifacts produced by dental materials. *American Journal of Neuroradiology*, **8**, 837-840.

Jackson, J.D. (1975) *Classical electrodynamics.* John Wiley.

Li, S. *et al.* (1995) A computer simulation of the static magnetic field distribution in the human head. *Magnetic Resonance in Medicine*, **34**, 268-275 .

LUDEKE, K.M. *et al.* (1985) Susceptibility artifacts in NMR imaging. *Magnetic Resonance Imaging*, **3**, 329-343.

MORRIS, P.G. (1982) *Nuclear Magnetic Resonance in medicine and biology.* Clarendon Press.

OLSSON, M. *et al.* (1995) A computer simulation program for MR imaging: application to RF and static magnetic field imperfections. *Magnetic Resonance in Medicine*, **34**, 612-617.

SCHENCK, J.F. (1996) The role of magnetic susceptibility in magnetic resonance imaging. *Medical Physics*, **23**, 815-850.

SCHWARTZ, L. (1966) *Mathematics for the physical sciences.* Hermann.

SEBASTIANI, G. & BARONE, P. (1991) Mathematical principles of basic magnetic resonance imaging in medicine. *Signal Processing*, **25**, 227-250.

SLICHTER, C.P. (1990) *Principles of magnetic resonance.* Springer Verlag.

WEIS, J. & BUDINSKY, L. (1990) Simulation of the influence of magnetic field inhomogeneities and distortion correction in MR imaging. *Magnetic Resonance Imaging*, **8**, 483-489.